ACS OMEGA

Open Access

http://pubs.acs.org/journal/acsodf

Article

Synergistic Effects of Carbon Vacancies in Conjunction with Phosphorus Dopant across Bilayer Graphene for the Enhanced Hydrogen Evolution Reaction

Huimin Hu and Jin-Ho Choi*

Cite This: *ACS Omega* 2024, 9, 16592−16600

Read Online

ACCESS | Metrics & More | Article Recommendations | Supporting Information

ABSTRACT: Bilayer graphene (BLG) exhibits distinct physical properties under external influences, such as torsion and structural defects, setting it apart from monolayer graphene. In this study, we explore the synergistic effects of carbon vacancies, in conjunction with phosphorus dopants, across BLG, focusing on their impact on structural, magnetic, electrical, and hydrogen adsorption properties. Our findings reveal that the substitutional doping of a phosphorus atom into a single carbon vacancy in a graphene layer induces substantial structural distortion in BLG. In contrast, doping phosphorus into a double vacancy maintains the flat structure of graphene layers. These distinct layer structures affect the electron distribution and spin arrangement, leading to varied electronic configurations and intriguing magnetic behaviors. Furthermore, the presence of abundant unsaturated electrons around the vacancy promotes the capture and bonding of hydrogen atoms. Hydrogen adsorption on BLG results in substantial orbital hybridization, accompanied by significant charge transfer. The calculated Gibbs free energies for hydrogen adsorption on BLG range from −0.08 to 0.09 eV, indicating exceptional catalytic activity for the hydrogen evolution reaction. These findings carry implications for optimizing the properties of graphene layers, making them highly desirable for applications such as catalysis.

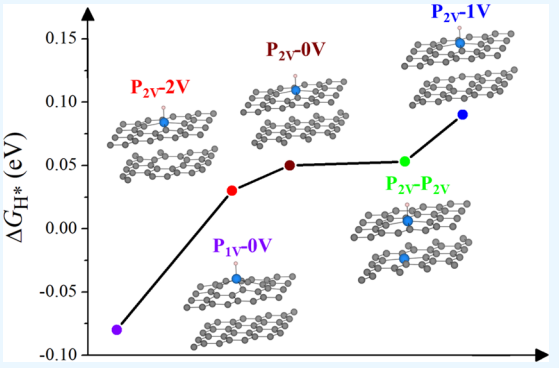

1. INTRODUCTION

Graphene, as the pioneering monolayer two-dimensional (2D) material successfully synthesized, stands out prominently within the realm of 2D materials.[1,2] Comprising single-atom-thick hexagonal carbon structures, graphene's carbon atoms engage in sp^2 orbital hybridization, forming a π-bond on the surface. This unique electronic configuration results in a distinctive energy band structure characterized by a zero band gap and Dirac cone, contributing significantly to graphene's exceptionally high electron mobility and electrical conductivity.[3−5] Moreover, graphene boasts a high specific surface area and exceptional light absorption properties, among other advantageous traits. These versatile features render graphene widely applicable in the fields of electronics, energy storage, and catalysis.[6,7]

It is crucial to recognize that the intrinsic monolayer graphene lacks inherent catalytic activity for producing hydrogen (H_2), a promising clean energy source. Currently, graphene is commonly employed as a substrate for active materials, forming a heterostructure catalyst. For instance, Chen et al. developed a nickel-doped molybdenum disulfide with graphene as a substrate, proving to be an efficient material for the hydrogen evolution reaction (HER) catalyst.[8] Wu et al. theoretically confirmed the positive role of graphene substrates in the catalytic behavior of GeP_3 and SnP_3 monolayers.[9]

Alternatively, graphene can undergo external modulation to finely adjust its electronic properties to amplify active sites and ultimately to enhance its intrinsic catalytic activity. Manipulating graphene by doping or introducing carbon vacancies stands as a widely employed strategy to improve its catalytic activity in H_2 production. For instance, Denis et al. investigated the dual-doped graphene systems and found that Al−O, S−N, P−O, and Si−B (para)-codoped graphene presented extraordinary chemical reactivity.[10] Zhang et al. proposed nitrogen, phosphorus, and fluorine tridoped graphene as a multifunctional catalyst, demonstrating outstanding catalytic properties for the oxygen reduction reaction (ORR), oxygen evolution reaction (OER), and HER.[11] Kumatani et al. revealed that the synergy of chemical doping and boundary engineering in graphene can significantly enhance its catalytic activity for HER.[12]

With extensive research on graphene, attention has gradually expanded to the study of bilayer graphene (BLG). In

Received: January 15, 2024
Revised: February 14, 2024
Accepted: March 19, 2024
Published: March 29, 2024

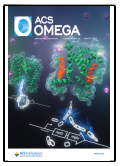

https://doi.org/10.1021/acsomega.4c00495
ACS Omega 2024, 9, 16592−16600

comparison to monolayer graphene, bilayer graphene possesses additional degrees of freedom such as stacking manners, interlayer spacing, and rotation angle between layers. These degrees of freedom contribute to the emergence of distinctive physical properties, enhancing the intrigue and fascination surrounding research on BLG. For example, the magic-angle graphene, achieved by precisely twisting BLG to a specific angle, triggers a strong correlation effect among electrons, leading to the manifestation of distinctive characteristics such as superconductivity and ferromagnetism.[13,14]

Bilayer graphene also holds promising applications in the field of energy storage and is anticipated to emerge as a favorable electrode material for secondary batteries.[15−17] Several studies on the fundamental properties of doped bilayer graphene have been reported previously.[18−21] Besides, bilayer graphene codoped with FeN_4−HfN_4 and FeN_4−IrN_4 has been reported for its remarkable catalytic prowess in the realms of HER, OER, and ORR.[22] The bilayer heterojunction composed of CoN_4-embedded graphene and B-doped graphene has been documented to exhibit outstanding oxygen reduction electrocatalytic activity.[23] Recently, it was reported that phosphorus-doped monovacancy at the hollow site of bilayer graphene is a promising alternative to Pt/C catalysts under acidic conditions for the oxygen reduction reaction (ORR).[24]

Applying high-energy atomic/ion bombardment to graphene layers can generate C (mono- and bi-) vacancies, enabling the relatively high-energy process of single-atom doping.[25−28] Consequently, the synthesis of P-doped graphene layers is feasible, and the creation of a composite material consisting of both P-doped and defective graphene layers is within reach.[29−31]

In contrast to single metal atom catalysts, nonmetallic single-atom catalysts demonstrate heightened stability and durability during catalytic reactions. Moreover, nonmetallic atoms offer environmental friendliness and cost-effectiveness in both preparation and utilization processes, further emphasizing their advantageous characteristics.[32] However, thus far, research on nonmetallic atom-doped BLG in the field of HER catalysis remains scarce. Furthermore, defective configurations in BLG, along with the resulting structural characteristics and significant changes in physical properties, have garnered substantial interest due to their potential impact on HER catalysis.

In this study, we explore the collaborative effects of phosphorus doping and carbon vacancies on the structural, magnetic, electronic, and catalytic properties of BLG by using first-principles density functional theory (DFT) calculations. The DFT calculations reveal that substituting a phosphorus (P) atom into the single carbon (C) vacancy of a graphene layer causes significant out-of-plane distortion in BLG, leading to nonflat layer structures. However, when doping occurs within a double C vacancy, the flat layer structure of graphene is well-preserved. These structural distortions also result in variations in the interlayer spacings of BLG. The interlayer interactions across BLG involving P dopants and C vacancies in different layers not only result in different geometrical configurations but also bestow distinct electronic, magnetic, and catalytic properties. Several combinations containing a P-doped layer exhibit outstanding catalytic activities for HER, as reflected by the H adsorption Gibbs free energies (−0.08−0.09 eV), approaching the optimal zero value. Hydrogen adsorption on BLG causes substantial orbital hybridization accompanied by significant charge transfer. These findings highlight the significant impact of interlayer interactions between the P dopant and C vacancies on the catalytic properties of graphene layers.

2. COMPUTATIONAL METHODS

Spin-polarized density functional theory (DFT) calculations were conducted using the Vienna Ab initio Simulation Package.[33] The calculations employed the projector-augmented wave method and the Perdew−Burke−Ernzerhof exchange−correlation functional. To include the effects of long-range van der Waals interactions, a semiclassical dispersion correction scheme (DFT-D3) was used.[34] The plane-wave cutoff energy was set to 550 eV. In structural optimization, all atoms underwent full relaxation until the forces acting on each atom reached values less than 0.01 eV/Å, adhering to the energy convergence criterion of 1×10^{-7} eV. We constructed a 4 × 4 supercell for the defective BLG, utilizing a 5 × 5 × 1 mesh to sample the 2D Brillouin zone.

The configurations of BLG with C vacancies and P dopants fall into four groups: (1) configurations with C vacancies only, (2) a single graphene layer doped with P, (3) two graphene layers doped with P, and (4) BLG with interstitial P doping. These BLG configurations are denoted by the number of C vacancies and the presence of a P dopant, 0V-1V represents a BLG configuration with one layer without a C vacancy and the other layer with one C vacancy, while P_{2V}-1V signifies a BLG configuration with one layer having P doped substitutionally into a double C vacancy and the other layer with a single C vacancy. Additionally, BLG with interstitial P doping is denoted by BLG-P.

The interlayer binding energy per atom (E_B) was calculated using the equation: $E_B = (E_{D\text{-}BLG} - E_{1L} - E_{2L})/N$, where $E_{D\text{-}BLG}$, E_{1L}, and E_{2L} is the total energy of defective BLG (D-BLG) and first and second graphene layer of D-BLG, respectively, and N represents the total atom number in D-BLG.

The formation energy (E_F) of defects in BLG is defined as

$$E_F = E_{D\text{-}BLG} - N_p\mu_p + N_c\mu_c - E_{BLG}$$

Here, E_{BLG} represent the total energy of BLG, N_p and N_c represent the number of P dopants and carbon vacancies, respectively, μ_p is the energy of single phosphorus atom in its bulk structure, and μ_c is per carbon atom in pristine graphene.

The H adsorption energy, denoted as ΔE_H, is defined as the difference between the total energy of the investigated BLG system with adsorbed H (E_{sys+H}), the total energy of the corresponding BLG system without H (E_{sys}), and half of the total energy of H_2 (E_{H_2}). This is expressed by the formula

$$\Delta E_H = E_{sys+H} - E_{sys} - \frac{1}{2}E_{H_2}$$

The overall HER reaction process begin with the Volmer reaction, expressed as $H^+ + e^- + * \rightarrow H^*$. In this context, H^+, e^-, * and H* represent the proton, electron, the active site, and the adsorbed H, respectively. Subsequently, the Tafel ($H^* + H^+ + e^- \rightarrow H_2$) or Heyrovsky reactions ($H^* + H^* \rightarrow H_2$) take place.[35] The Volmer reaction, recognized as the most critical component in the HER, can be evaluated through the assessment of the H adsorption Gibbs free energy (ΔG_H), calculated by $\Delta G_H = \Delta E_H + \Delta E_{ZPE} - T\Delta S$. ΔE_{ZPE} denotes the zero-point energy correction for H_2, while ΔS signifies the entropy difference between the adsorbed H atom and molecule

https://doi.org/10.1021/acsomega.4c00495
ACS Omega 2024, 9, 16592−16600

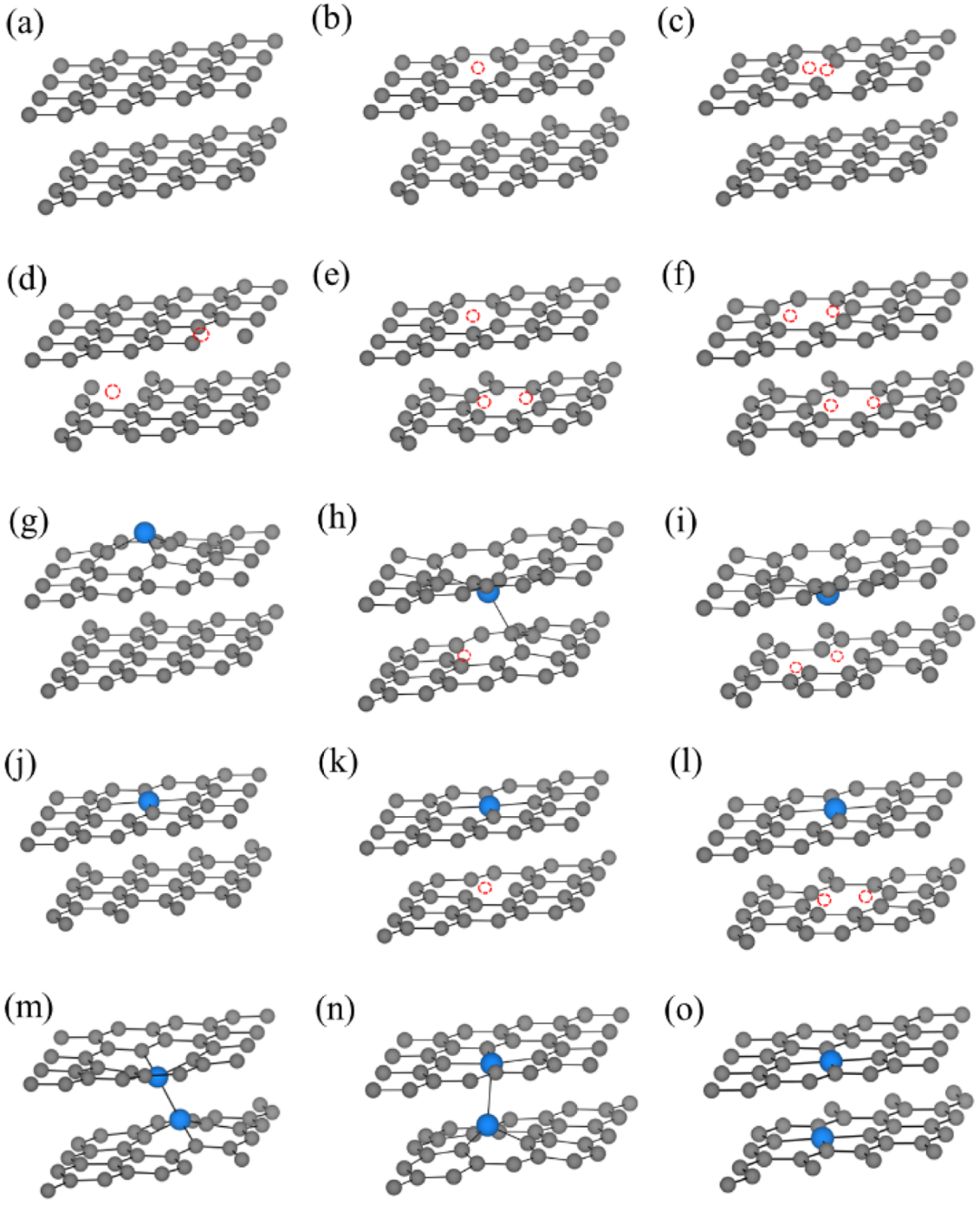

Figure 1. Optimized atomic geometries for (a) pristine BLG and defective BLG with a P dopant or C vacancies: (b) 1V−0V, (c) 2V−0V, (d) 1V−1V, (e) 1V−2V, (f) 2V−2V; (g) P_{1V}-0V, (h) P_{1V}-1V, (i) P_{1V}-2V, (j) P_{2V}-0V, (k) P_{2V}-1V, (l) P_{2V}-2V, (m) P_{1V}-P_{1V}, (n) P_{2V}-P_{1V}, and (o) P_{2V}-P_{2V} configurations. Gray and blue circles represent C and P atoms, respectively. The locations of the C vacancies are marked by red dashed circles.

in the gas phase under the standard conditions. This relationship is expressed by the formula

$$\Delta S = \frac{1}{2} S^0_{H_2}$$

where $S^0_{H_2}$ is the entropy of a H_2 gas molecule.[36]

3. RESULTS AND DISCUSSION

The investigation commenced with an analysis of pristine BLG. Figure 1a displays the optimized structure of the AB-stacked BLG. The pristine BLG exhibits nonmagnetic properties, with an interlayer spacing of 3.38 Å and a calculated interlayer binding energy of −24 meV/per atom, consistent with previous studies.[37−41] Subsequently, our investigation explores the impact of C vacancies and P doping on the structural and energetic properties. Figure 1b−f highlights the lowest energy configurations when introducing only C vacancy (XV-YV, see the Computational Methods section for notation), revealing a slight increase in layer spacing by only 0.02−0.06 Å compared to pristine BLG. It is noteworthy that the flat layered structure is maintained. The interlayer binding energy changes slightly compared to that of pristine BLG, by −2.97 to 2.3 meV. For P

https://doi.org/10.1021/acsomega.4c00495
ACS Omega 2024, 9, 16592−16600

Table 1. C Interlayer Spacing (d), Magnetic Moment (M), Relative Interlayer Binding Energy Per Atom (ΔE_B), Defective Formation Energy (E_F), H Adsorption Energy (ΔE_H) and Corresponding Free Energy (ΔG_H) on Extralayer (Interlayer) in BLG Configurations with and without Defects[a]

	d (Å)	M (μB)	ΔE_B (meV)	E_F (eV)	ΔE_H (eV)	ΔG_H (eV)
BLG	3.38	0	0		1.37 (1.5)	1.6 (1.74)
1V-0V	3.41	1.54	0.042	7.94	−1.17	−0.93
2V-0V	3.42	0	0.58	8.56	−0.8	−0.56
1V-1V	3.4	3.36	−2.97	15.73	−1.11	−0.87
1V-2V	3.44	1.52	2.3	16.46	−1.94	−1.7
2V-2V	3.41	0	1.23	17.12	−0.43	−0.19
P_{1V}-0V	3.35	1	−0.37	2.83	−0.32 (1.2)	−0.08 (1.44)
P_{1V}-1V	3.56	0.71	−23.74	9.27	0.22 (−1.32)	0.46 (−1.08)
P_{1V}-2V	3.54	0	21.62	11.22	−0.03 (−2.09)	0.21 (−1.85)
P_{2V}-0V	3.4	0	0.82	4.1	−0.19 (−0.01)	0.05 (0.23)
P_{2V}-1V	3.38	1.12	−1.87	11.92	−0.15 (−1.88)	0.09 (−1.64)
P_{2V}-2V	3.42	0	3.12	12.7	−0.21 (−0.82)	0.03 (−0.58)
P_{1V}-P_{1V}	3.89	0	1.23	5.68	0.04 (1.4)	0.28 (1.64)
P_{1V}-P_{2V}	3.46	0	−13.66	6.17	0.21 (0.76)	0.45 (1.0)
P_{2V}-P_{2V}	3.38	0	10.01	8.16	−0.187 (−0.08)	0.053 (0.16)
BLG-P	4.89	1		4.76	0.04 (−1.26)	0.28 (−1.02)

[a]For ΔE_B, the value of the pristine BLG is set to zero.

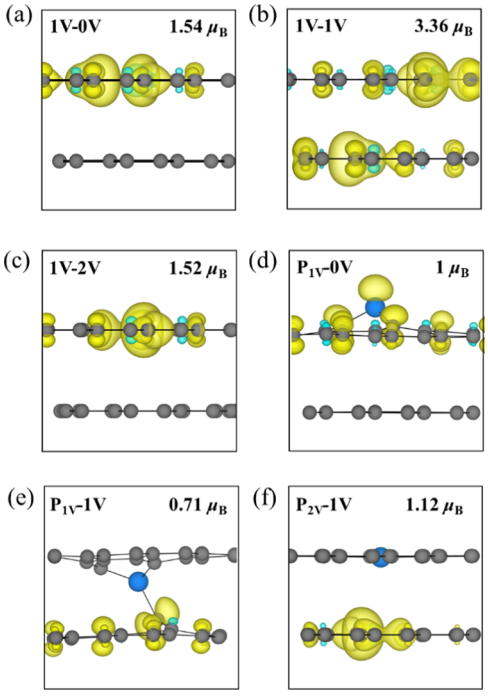

Figure 2. Spin density results for magnetic BLG configurations. The yellow isosurface is drawn at a density of 0.004 e Å^{-3}.

doping, the BLG structure depends highly on the number of C vacancies of the P-doped layer: BLG containing a layer with P doped substitutionally into a single C vacancy (denoted as P_{1V}) undergoes substantial structural distortion, while BLG with P_{2V} layers maintains the flat layered structure. This trend is because double C vacancy can offer ample space for P doping.

The concurrent presence of a P dopant and C vacancies induces variation in the interlayer spacing of BLG, ranging from 3.35 to 3.89 Å. Simultaneously, the interlayer binding energy changes from −23.74 to 21.62 meV, as detailed in Table 1. To provide a comprehensive understanding, we also explored interstitial P doping between layers of BLG (BLG-P), as illustrated in Figure S1. The BLG-P configuration demonstrates a substantial increase in the interlayer spacing, measuring 4.89 Å. The P dopant in the P_{1V} layer tends to be located toward to the C vacancies of the other layer, as shown in Figure 1h,i. This is in sharp contrast to the case of P_{1V}-0V, where P protrudes outward of BLG (Figure 1g). The trend is understandable because C vacancies possess dangling bonds that are known to often attract other atoms or molecules with unsaturated electron configurations, such as P.[42,43]

The formation energy (E_F) of defects in BLG was investigated to determine the stability of the defective BLG configurations. The calculated E_F values, as listed in Table 1, for all of the considered defective BLG configurations are positive, indicating that the formation of defects in BLG is endothermic. The difference in the E_F between 1V-0V and 2V-0V (7.94 and 8.56 eV, respectively) is only 0.62 eV, suggesting that inducing a second C vacancy is facilitated when a single vacancy exists. The formation energy of P_{1V}-0V is 2.83 eV, considerably lower than those of P_{2V}-0V (4.1 eV) and BLG-P (4.76 eV), indicating that substitutional P doping into a single C vacancy is energetically more favorable.

The distinct structural features arising from different doping and vacancy configurations led to varying magnetic properties. It is widely recognized that a C vacancy within a graphene layer leads to the emergence of magnetic moments, stemming from the presence of unpaired electrons surrounding the defect.[44] The calculated magnetic moment in this work is 1.53 μ_B, consistent with previous studies.[45] In contrast, within a graphene layer containing a double C vacancy, these localized magnetic moments vanish. This occurs due to an even number of dangling bonds, allowing for the pairing of all unpaired electrons. Consequently, the total magnetic moment becomes zero. For the BLG, our DFT calculations revealed similar magnetic trends. The magnetic moments for the 1V-0V (Figure 2a) and 1V-2V (Figure 2c) configurations are nearly identical, measuring 1.54 μ_B and 1.52 μ_B, respectively. Notably, the magnetic moment of 1V-1V is slightly higher than twice the value of a single 1V layer (3.36 μ_B), implying the effects of interlayer interactions.

https://doi.org/10.1021/acsomega.4c00495
ACS Omega 2024, 9, 16592−16600

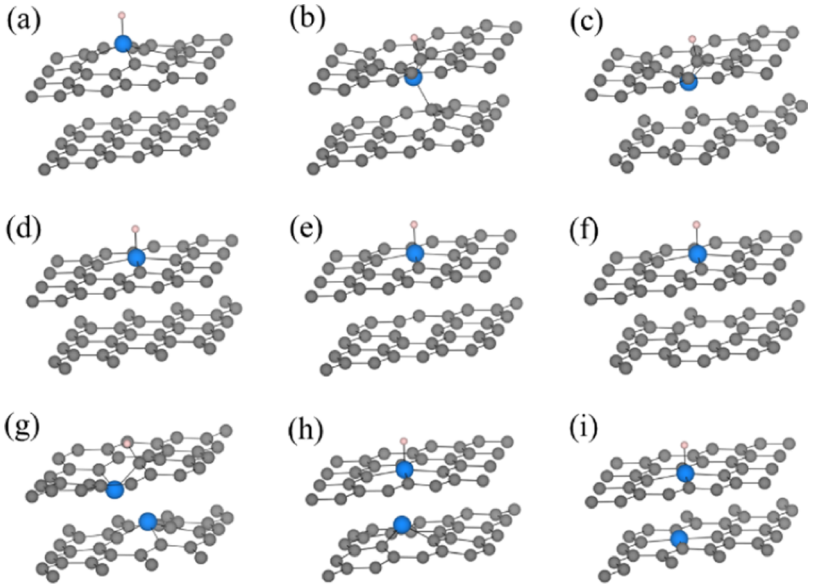

Figure 3. Optimized hydrogen adsorption configurations on the surface of (a) P_{1V}-0V, (b) P_{1V}-1V, (c) P_{1V}-2V, (d) P_{2V}-0V, (e) P_{2V}-1V, and (f) P_{2V}-2V, (g) P_{1V}-P_{1V}, (h) P_{2V}-P_{1V}, and (i) P_{2V}-P_{2V}. Gray, blue, and pink circles represent C, P, and H atoms, respectively.

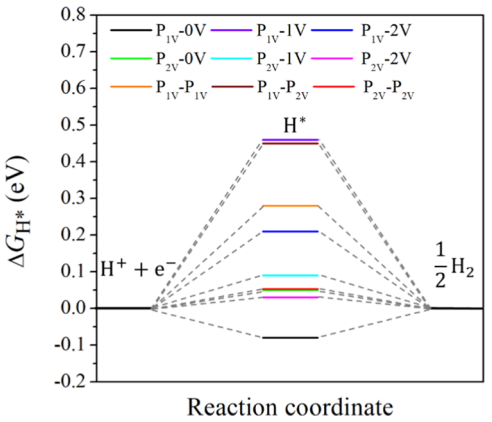

Figure 4. Calculated hydrogen adsorption Gibbs free energy values (ΔG_H) for the configurations with concurrent presence of the P dopant and C vacancies. The ΔG_H in P_{1V}-0V, P_{2V}-0V, P_{2V}-1V, P_{2V}-2V, and P_{2V}-P_{2V} are close to 0 eV, where H adsorbed at the top site of P.

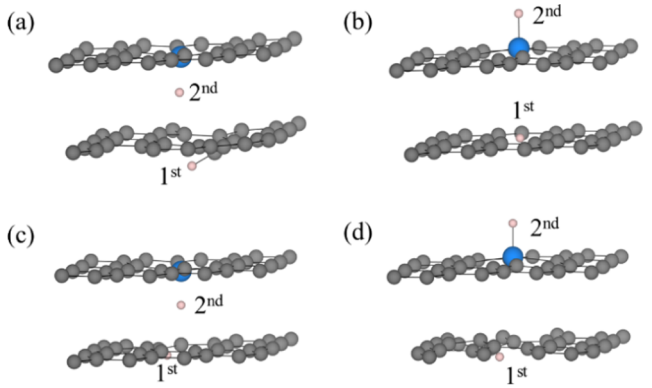

Figure 5. Adsorption configuration of the two H atoms in P_{2V}-1V and P_{2V}-2V, where the first H atom adsorbs on the vacancy sites and the second H atom adsorbs on the (a) inner and (b) outer surfaces of P_{2V}-1V and the (c) inner and (d) outer surfaces of P_{2V}-2V.

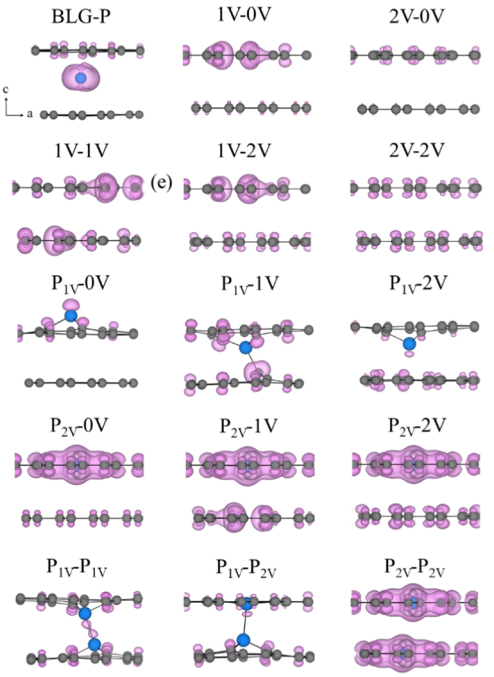

Figure 6. Partial electron densities obtained from the states within the energy range of E_F −1 eV < E < E_F. The iso-surfaces were taken at charge densities of 0.008 e Å^{-3}.

We now investigate the effects of P doping on the magnetic properties of BLG. In the P_{1V}-0V configuration (Figure 2d), three of the valence electrons in P form three σ bonds with the neighboring C atoms, while the fourth replaces the missing C and forms one π bond. The remaining one unpaired valence electron exists as a lone pair and reduces the magnetic moment to 1 μ_B. Interestingly, the interlayer interactions of the P-doped P_{1V} and defective 1V layers result in an interlayer ferrimagnetic spin ordering with opposite spin orientations, as illustrated in Figure 2e. The total magnetic moment of P_{1V}-1V is 0.71 μ_B, even lower than that of P_{1V}-0V. When combined with the nonmagnetic 2V layer, the P_{1V} layer also becomes nonmagnetic

https://doi.org/10.1021/acsomega.4c00495
ACS Omega 2024, 9, 16592−16600

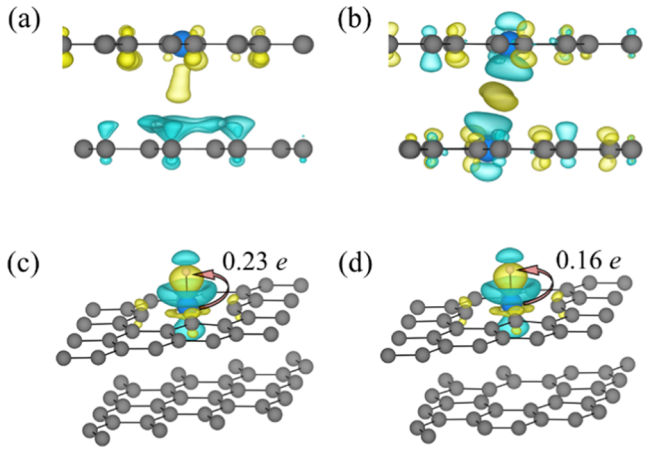

Figure 7. Differential charge density plots for (a, c) P_{2V}-0V and (b, d) P_{2V}-2V before and after H adsorption. The yellow and blue isosurfaces are drawn at the density of 0.0003 and −0.0003 e Å^{-3} for (a, b) and 0.0004 and −0.0004 e Å^{-3} for (c, d), respectively.

following the 2V layer. The unsaturated electrons of P are uniformly transferred to the four C atoms around the vacancies in the 2V layer. As a result, the total magnetic moment of P_{1V}-2V is zero. Similarly, the P-doped 2V layer (P_{2V}) is nonmagnetic with zero magnetic moment. The defect geometry of the 2V layer significantly affects the bonding configuration of the P dopant in the layer. The five valence electrons of P are saturated by forming four C−P σ bonds and one π bond, resulting in no unpaired electron. Therefore, in BLG with P_{2V}-0V and P_{2V}-2V configurations, the magnetic moments are zero. In contrast, P_{2V}-1V exhibits a nonzero magnetic moment of 1.12 μ_B, mainly distributed around a single vacancy in the 1V layer (see Figure 2f).

The interlayer interactions between two P dopants across the BLG can affect the magnetic ordering. For example, although P_{1V} alone has a magnetic moment of 1 μ_B, BLG with both P_{1V}-P_{2V} and P_{1V}-P_{1V} configurations exhibit zero magnetic moments. When a P_{1V} layer with unsaturated electrons encounters a structurally symmetrical P_{2V} layer, the resulting nonmagnetic behavior aligns with that of P_{1V}-2V. Nevertheless,

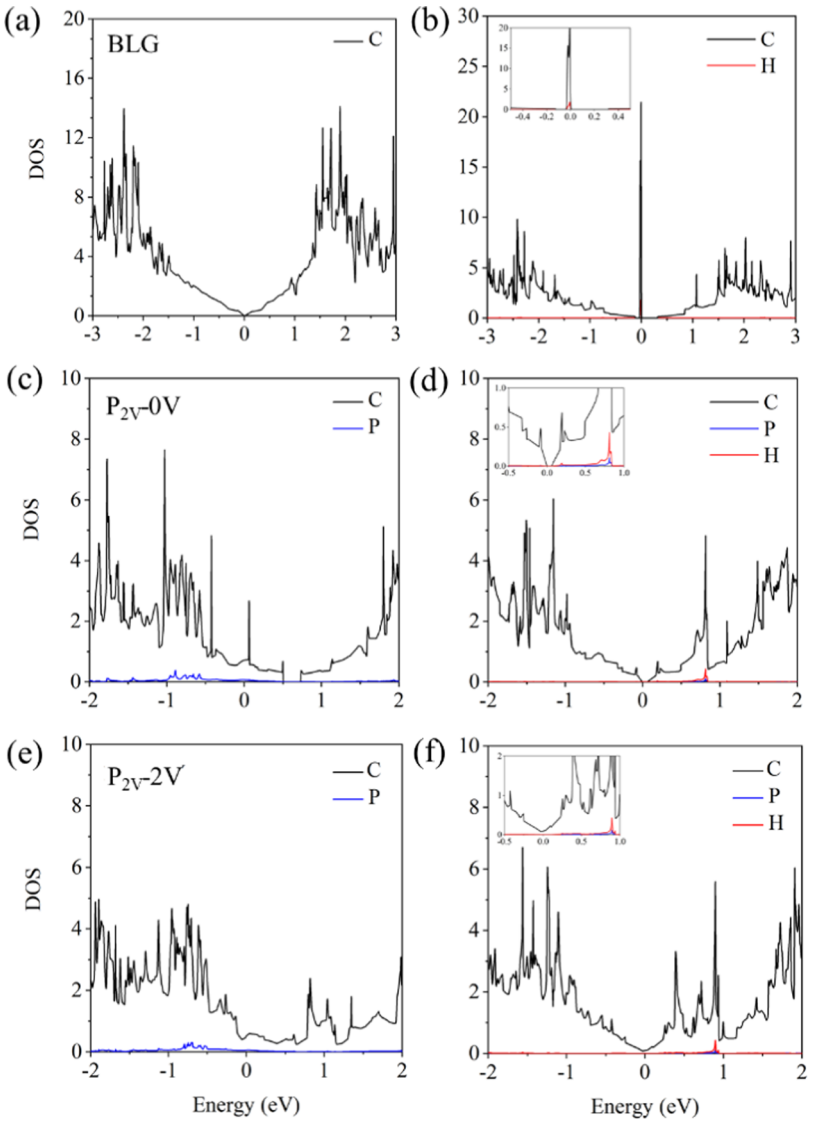

Figure 8. Calculated density of states for (a) BLG, (b) H adsorption on BLG, (c) P_{2V}-0V, (d) H adsorption on P_{2V}-0V, (e) P_{2V}-2V, and (f) H adsorption on P_{2V}-2V. The Fermi energy level is set to be 0 eV.

https://doi.org/10.1021/acsomega.4c00495
ACS Omega 2024, 9, 16592−16600

in the scenario where two P_{1V} layers with unsaturated electrons converge, the symmetrical configuration between the layers results in the charge transfer between P atoms to form a P−P bond. This interlayer interaction renders the P_{1V}-P_{1V} system showcasing a lack of magnetism.

In contrast, the flat P_{2V}-P_{2V} configuration, distinguished by the absence of redundant electrons, inherently exhibits a nonmagnetic nature. However, in the case of BLG-P, the magnetic moment with 1 μ_B becomes localized around the P atom, as illustrated in Figure S2. This phenomenon is attributed to the presence of one excess unsaturated electron associated with the P atom.

In our investigation of H adsorption on various defective BLG configurations, we further observe a significant enhancement in adsorption strength compared to pristine BLG. Specifically, in the case of interstitial P doping (BLG-P), H atoms exhibit the formation of a strong C−P bond with the interstitially doped P, as indicated by the H adsorption energy (ΔE_H) of −1.26 eV. Furthermore, interstitial P doping enhances H adsorption on BLG surfaces, with a calculated ΔE_H of 0.04 eV—significantly lower than the value (1.5 eV) observed in pristine BLG. In BLG with C vacancies, H atoms tend to adsorb onto vacancies within the graphene layer, as illustrated in Figure S3. All configurations display robust C−H bonds, with ΔE_H ranging from −1.94 to −0.43 eV.

When P doping is introduced into the C vacancies of BLG, the H adsorption properties are examined in both the outer surface and inner surface. In cases where the P-doped layer coexists with the vacancy layer, the adsorption of H atoms on the inner surfaces tends to occur at the vacancy sites within the vacancy layer, as illustrated in Figure S4. The ΔE_H values for P_{1V}-1V, P_{1V}-2V, P_{2V}-1V, and P_{2V}-2V are −1.32, −2.09, −1.88, and −0.82 eV, respectively. In contrast, for the configurations consisting solely of P-doped or pristine graphene layers (P_{1V}-0V, P_{2V}-0V, P_{1V}-P_{1V}, P_{2V}-P_{2V}, P_{1V}-P_{2V}), the inner-surface H adsorption is relatively weak, as reflected by ΔE_H ranging from 1.4 to −0.08 eV. Interestingly, we observe that in the BLG configurations involving a P-doped layer with P_{1V}, where the P dopant is located toward the other layer, the H atoms adsorbed on the outer surface tend to form tilted C−H bonds with the C atoms around P (see Figure 3b,c,g). On the contrary, in the other configurations, the adsorbed H atoms adhere to the P top site of the P_{2V} layer (Figure 3d−f,h,i). Additionally, H atoms adsorbed on the outer surface exhibit relatively weakened adsorption compared to adsorption on the inner surface in configurations containing both vacancy and P-doped layers. More importantly, for the P_{1V}-0V, P_{2V}-0V, P_{2V}-1V, P_{2V}-2V, and P_{2V}-P_{2V} configurations featuring H adsorption at the P top site, the corresponding adsorption Gibbs free energy values (ΔG_H) range from −0.08 to 0.05 eV, which closely approaches the optimal value (ΔG_H = 0 eV) for HER, as shown in Table 1 and Figure 4. These results suggest their potential as promising hydrogen catalysts.

Given that the H atoms adsorbed on the inner surface in P_{2V}-1V and P_{2V}-2V form robust C−H bonds with C in the vacancy layer, our subsequent investigation delves into the adsorption of the second H atom. In P_{2V}-1V, the ΔE_H of the second H atom on the P top site (outer surface) is −0.11 eV, slightly higher than that (−0.15 eV) of the first H atom. On the other hand, the adsorption of the second H atom on the inner surface causes substantial structural distortion in the 1V layer due to the repulsive interactions between the two adsorbed H, as shown in Figure 5a. The calculated ΔE_H is −0.98 eV, indicating that the inner-surface adsorption of the second H atom is stronger than that of the outer surface. For P_{2V}-2V, the corresponding ΔE_H of the outer (inner) surface is 0.17 (−0.21) eV. As a result, ΔG_H closest to the optimal zero value is 0.03 eV for P_{2V}-2V (inter surface) and 0.13 eV for P_{2V}-1V (outer surface), suggesting that these configurations can still provide activity sites for other H atoms in the presence of already adsorbed H in the vacancy graphene layer.

Our subsequent investigation reveals that distinct H adsorption behaviors of the different defect configurations are intricately linked to the electron distribution in the occupied states near the Fermi level. The partial electron density plot in Figure 6 indicates that, in comparison, the 1V configuration possesses the densest electron density around the vacancy site, followed by 2V, while the charge around the 0V configuration is nearly negligible. The abundant electron distribution serves as an active site, attracting hydrogen atoms for reaction and forming strong C−H bonds. Under the influence of P, the P_{1V} layer in various defective BLG configurations manifests distinct charge distributions. In the P_{1V}-0V configuration, electrons are primarily distributed around the P dopant. In the P_{1V}-1V configuration, the P dopant located toward the inner side of BLG induces charge localization at the C atoms around P and the C vacancy in the 1V layer. The electrons are more localized compared with those of P_{1V}-2V. The localized electron distribution results in the formation of robust C−H bonds. The P_{2V} layer shows 4-fold symmetric charge distribution that is primarily concentrated around the P dopant, which accounts for the fact that P is the most favorable site for the H adsorption. In contrast, P_{2V}-0V, P_{2V}-1V, and P_{2V}-2V configurations display distinguishing electron distribution mainly within the vacancy layer. As the 1V layer possesses a higher electron density, it demonstrates the most robust H adsorption in P_{2V}-1V. Overall, the notable electron distribution on C atoms surrounding the vacancy results in the formation of strong C−H bonds, aligning with the calculated ΔE_H.

The P_{1V}-P_{1V} and P_{1V}-P_{2V} configurations have less electronic states near the Fermi level, which can account for their higher ΔE_H. The charge distribution in the P_{2V} layer in P_{2V}-P_{2V} is nearly identical to that in P_{2V}-0V. Consequently, these two configurations demonstrate nearly identical hydrogen adsorption behavior on the P_{2V} surface, including the preferred H adsorption site and adsorption strength.

The outstanding catalytic activities of P_{2V}-0V and P_{2V}-2V can be interpreted by significant charge transfer. The differential charge density plots in Figure 7a,b highlight considerable charge transfer in P_{2V}-0V and P_{2V}-2V across BLG. Upon H adsorption, substantial charge transfer occurs between the P dopant and adsorbed H atom, as shown in Figure 7c,d. Our Bader charge analysis reveals that in P_{2V}-0V (P_{2V}-2V), the H atom gains 0.4e (0.335e), while the P dopant loses 0.23e (0.16e). The appropriate amount of charge transfer between the H and P atoms results in a moderate H adsorption strength, which is desirable for the HER.

The density of states (DOS) reveals that the states near the Fermi level originate primarily from C vacancies and P dopants in P_{2V}-0V and P_{2V}-2V. These electronic structures facilitate orbital hybridization with H atoms, leading to the adsorption preference on the vacancy and dopant. In contrast to the narrow-gap semiconducting characteristics of pristine BLG (Figure 8a), the P_{2V}-0V configuration exhibits an upward shift of the valence band maximum, increasing the DOS at E_F

https://doi.org/10.1021/acsomega.4c00495
ACS Omega 2024, 9, 16592−16600

(Figure 8c). The calculated band gaps for pristine BLG and P_{2V}-0V are 0.019 and 0.23 eV, respectively. In contrast, the P_{2V}-2V configuration is completely metallic (Figure 8e). The H adsorption gives rise to a prominent peak at the E_F in BLG (Figure 8b), signifying the presence of highly localized electrons. This suggests a subtle orbital hybridization between the adsorbed H atoms and the C atom of the adsorption site. In contrast, P_{2V}-0V and P_{2V}-2V show no prominent peak at the Fermi level due to substantial orbital hybridization of P and H. As depicted in Figure 8d,f, the projected densities of states of P and H align well with each other, indicating s−p orbital hybridization. This interaction weakens the electronic hybridization between P and C, resulting in a downward shift of the C states near the Fermi level.

4. CONCLUSIONS

In summary, we have investigated the collaborative effects of P doping and C vacancies on the structural, magnetic, electronic, and catalytic properties of BLG. The findings reveal that the P dopants within the P_{1V} layer tend to be situated toward the inner layer of BLG, while the P_{2V} layer maintains a flat configuration. The distinct defective configurations result in varied electron distribution, giving rise to intriguing magnetic behaviors. Notably, the electron distribution near the Fermi level has a crucial impact on H adsorption behavior. More importantly, P_{1V}-0V, P_{2V}-0V, P_{2V}-1V, P_{2V}-2V, and P_{2V}-P_{2V} exhibited ΔG_H close to 0, with H adsorb at the top site of P, signifying excellent catalytic activity for HER. Further investigations demonstrate that the charge transfer between H atoms and adsorbed P atoms plays a facilitating role in the catalytic reaction. It is also noteworthy that, in the scenario where a H atom initially occupies the vacancy site in the 2V layer of P_{2V}-1V and P_{2V}-2V, the catalytic activity remains excellent for the second H adsorption. These findings suggest that structural changes by the interactions of the P dopant and C vacancies also modify the electronic distribution and spin ordering significantly. This work offers implications for the application of graphene layers in HER catalysis.

■ ASSOCIATED CONTENT

Supporting Information

The Supporting Information is available free of charge at https://pubs.acs.org/doi/10.1021/acsomega.4c00495.

The optimized configuration and spin density results of BLG-P and H adsorption configurations in BLG with the vacancy layer (PDF)

■ AUTHOR INFORMATION

Corresponding Author

Jin-Ho Choi − *College of Energy, Soochow Institute for Energy and Materials Innovations, Soochow University, Suzhou 215006, China; Key Laboratory of Advanced Carbon Materials and Wearable Energy Technologies of Jiangsu Province and Key Laboratory of Core Technology of High Specific Energy Battery and Key Materials for Petroleum and Chemical Industry, Soochow University, Suzhou 215006, China; Key Laboratory of Advanced Negative Carbon Technologies, Soochow University, Suzhou 215123, China;* orcid.org/0000-0001-6498-2929; Email: jhchoi@suda.edu.cn

Author

Huimin Hu − *College of Energy, Soochow Institute for Energy and Materials Innovations, Soochow University, Suzhou 215006, China; Key Laboratory of Advanced Carbon Materials and Wearable Energy Technologies of Jiangsu Province and Key Laboratory of Core Technology of High Specific Energy Battery and Key Materials for Petroleum and Chemical Industry, Soochow University, Suzhou 215006, China; Key Laboratory of Advanced Negative Carbon Technologies, Soochow University, Suzhou 215123, China*

Complete contact information is available at: https://pubs.acs.org/10.1021/acsomega.4c00495

Notes

The authors declare no competing financial interest.

■ ACKNOWLEDGMENTS

This work was supported by the National Natural Science Foundation of China (Grants No. 11874044 and No. 52350610260). The calculations were performed on TianHe-1(A) at the NSCC in Tianjin.

■ REFERENCES

(1) Tiwari, S. K.; Sahoo, S.; Wang, N.; Huczko, A. Graphene research and their outputs: Status and prospect. *J. Sci.: Adv. Mater. Devices* **2020**, *5* (1), 10−29.

(2) Edwards, R. S.; Coleman, K. S. Graphene synthesis: relationship to applications. *Nanoscale* **2013**, *5* (1), 38−51.

(3) Novoselov, K. S.; Geim, A. K.; Morozov, S. V.; Jiang, D.; Katsnelson, M. I.; Grigorieva, I. V.; Dubonos, S. V.; Firsov, A. A. Two-dimensional gas of massless Dirac fermions in graphene. *Nature* **2005**, *438* (7065), 197−200.

(4) Wang, G. X. A series of two-dimensional carbon allotropes with Dirac cone structure. *Phys. Chem. Chem. Phys.* **2023**, *25* (23), 15815−15821.

(5) Teng, C.; Xie, D.; Wang, J. F.; Yang, Z.; Ren, G. Y.; Zhu, Y. Ultrahigh Conductive Graphene Paper Based on Ball-Milling Exfoliated Graphene. *Adv. Funct. Mater.* **2017**, *27* (20), No. 1700240, DOI: 10.1002/adfm.201700240.

(6) Miller, D. L.; Kubista, K. D.; Rutter, G. M.; Ruan, M.; de Heer, W. A.; First, P. N.; Stroscio, J. A. Observing the Quantization of Zero Mass Carriers in Graphene. *Science* **2009**, *324* (5929), 924−927.

(7) Hirsch, A. The era of carbon allotropes. *Nat. Mater.* **2010**, *9* (11), 868−871.

(8) Chen, L. X.; Chen, Z. W.; Wang, Y.; Yang, C. C.; Jiang, Q. Design of Dual-Modified MoS_2 with Nanoporous Ni and Graphene as Efficient Catalysts for the Hydrogen Evolution Reaction. *ACS Catal.* **2018**, *8* (9), 8107−8114.

(9) Wu, H. H.; Huang, H.; Zhong, J.; Yu, S.; Zhang, Q.; Zeng, X. C. Monolayer triphosphates MP(3) (M = Sn, Ge) with excellent basal catalytic activity for hydrogen evolution reaction. *Nanoscale* **2019**, *11* (25), 12210−12219.

(10) Denis, P. A.; Pereyra Huelmo, C. Structural characterization and chemical reactivity of dual doped graphene. *Carbon* **2015**, *87*, 106−115.

(11) Zhang, J. T.; Dai, L. M. Nitrogen, Phosphorus, and Fluorine Tri-doped Graphene as a Multifunctional Catalyst for Self-Powered Electrochemical Water Splitting. *Angew. Chem., Int. Ed.* **2016**, *55* (42), 13296−13300.

(12) Kumatani, A.; Miura, C.; Kuramochi, H.; Ohto, T.; Wakisaka, M.; Nagata, Y.; Ida, H.; Takahashi, Y.; Hu, K.; Jeong, S.; Fujita, J. I.; Matsue, T.; Ito, Y. Chemical Dopants on Edge of Holey Graphene Accelerate Electrochemical Hydrogen Evolution Reaction. *Adv. Sci.* **2019**, *6* (10), No. 1900119.

(13) Wu, F. C.; Das Sarma, S. Ferromagnetism and superconductivity in twisted double bilayer graphene. *Phys. Rev. B* **2020**, *101* (15), No. 155149, DOI: 10.1103/PhysRevB.101.155149.
(14) Hsu, Y. T.; Wu, F. C.; Das Sarma, S. Topological superconductivity, ferromagnetism, and valley-polarized phases in moire systems: Renormalization group analysis for twisted double bilayer graphene. *Phys. Rev. B* **2020**, *102* (8), No. 085103, DOI: 10.1103/PhysRevB.102.085103.
(15) Ji, K. M.; Han, J. H.; Hirata, A.; Fujita, T.; Shen, Y.; Ning, S. C.; Liu, P.; Kashani, H.; Tian, Y.; Ito, Y.; Fujita, J.; Oyama, Y. Lithium intercalation into bilayer graphene. *Nat. Commun.* **2019**, *10*, No. 1603421, DOI: 10.1038/s41467-018-07942-z.
(16) Yang, S.; Fecher, S.; Wang, Q. X.; Kühne, M.; Smet, J. H. Device level reversible potassium intercalation into bilayer graphene. *2D Mater.* **2022**, *9* (2), No. 025020, DOI: 10.1088/2053-1583/ac58a1.
(17) Li, J. R.; Yang, S. B.; Zhang, X.; Zhang, C. X. Y. Exploring the effect of layer spacing of graphene for lithium single-atom diffusion using first principles calculations. *Comput. Theor. Chem.* **2022**, *1217*, No. 113937, DOI: 10.1016/j.comptc.2022.113937.
(18) Denis, P. A. Band gap opening of monolayer and bilayer graphene doped with aluminium, silicon, phosphorus, and sulfur. *Chem. Phys. Lett.* **2010**, *492* (4−6), 251−257.
(19) Denis, P. A.; Iribarne, F. The effect of the dopant nature on the reactivity, interlayer bonding and electronic properties of dual doped bilayer graphene. *Phys. Chem. Chem. Phys.* **2016**, *18* (35), 24693−703.
(20) Denis, P. A. Theoretical characterization of codoped bilayer graphene. *Comput. Theor. Chem.* **2023**, *1221*, No. 114035.
(21) Denis, P. A. When noncovalent interactions are stronger than covalent bonds: Bilayer graphene doped with second row atoms, aluminum, silicon, phosphorus and sulfur. *Chem. Phys. Lett.* **2011**, *508* (1−3), 95−101.
(22) Hu, R.; Li, Y.; Wang, F.; Shang, J. Rational prediction of multifunctional bilayer single atom catalysts for the hydrogen evolution, oxygen evolution and oxygen reduction reactions. *Nanoscale* **2020**, *12* (39), 20413−20424.
(23) Xiao, B. B.; Zhang, Z.; Yu, L. B.; Huang, Q. Y.; Wu, J.; Song, E. H.; Wang, L. L. Boosting oxygen reduction electrocatalysis of graphene-based bilayer heterojunction. *Surfaces and Interfaces* **2022**, *33*, No. 102232, DOI: 10.1016/j.surfin.2022.102232.
(24) Pham, N. N. T.; Nguyen, V. K. T.; Guo, H.; Lee, S. G. Influence of phosphorus-doped bilayer graphene configuration on the oxygen reduction reaction in acidic solution. *Carbon* **2023**, *210*, No. 118012, DOI: 10.1016/j.carbon.2023.118012.
(25) Wang, H.; Wang, Q.; Cheng, Y.; Li, K.; Yao, Y.; Zhang, Q.; Dong, C.; Wang, P.; Schwingenschlogl, U.; Yang, W.; Zhang, X. X. Doping monolayer graphene with single atom substitutions. *Nano Lett.* **2012**, *12* (1), 141−144.
(26) Ramasse, Q. M.; Seabourne, C. R.; Kepaptsoglou, D. M.; Zan, R.; Bangert, U.; Scott, A. J. Probing the Bonding and Electronic Structure of Single Atom Dopants in Graphene with Electron Energy Loss Spectroscopy. *Nano Lett.* **2013**, *13* (10), 4989−4995.
(27) Tripathi, M.; Markevich, A.; Böttger, R.; Facsko, S.; Besley, E.; Kotakoski, J.; Susi, T. Implanting Germanium into Graphene. *ACS Nano* **2018**, *12* (5), 4641−4647.
(28) Ullah, S.; Shi, Q.; Zhou, J.; Yang, X.; Ta, H. Q.; Hasan, M.; Ahmad, N. M.; Fu, L.; Bachmatiuk, A.; Rümmeli, M. H. Advances and Trends in Chemically Doped Graphene. *Adv. Mater. Interfaces* **2020**, *7* (24), No. 105021, DOI: 10.1002/admi.202000999.
(29) Rao, Y.; Yuan, M.; Luo, F.; Wang, Z.; Li, H.; Yu, J.; Chen, X. One-step laser fabrication of phosphorus-doped porous graphene electrodes for high-performance flexible microsupercapacitor. *Carbon* **2021**, *180*, 56−66.
(30) Feng, L.; Qin, Z.; Huang, Y.; Peng, K.; Wang, F.; Yan, Y.; Chen, Y. Boron-, sulfur-, and phosphorus-doped graphene for environmental applications. *Sci. Total Environ.* **2020**, *698*, No. 134239.
(31) Zhan, X.; Tong, X.; Gu, M.; Tian, J.; Gao, Z.; Ma, L.; Xie, Y.; Chen, Z.; Ranganathan, H.; Zhang, G.; Sun, S. Phosphorus-Doped Graphene Electrocatalysts for Oxygen Reduction Reaction. *Nanomaterials* **2022**, *12* (7), No. 1141, DOI: 10.3390/nano12071141.
(32) Zhang, F.; Zhang, Q. J.; Chen, Y. C.; Xu, L. Y.; Li, Z. L.; Wang, Q. T.; Zhang, Q. F.; Li, X. N. Advances and mechanistic insights in the catalytic semi-hydrogenation of acetylene over non-metallic catalysts. *Appl. Catal., A* **2023**, *667*, No. 119447, DOI: 10.1016/j.apcata.2023.119447.
(33) Kresse, G.; Furthmuller, J. Efficiency of ab-initio total energy calculations for metals and semiconductors using a plane-wave basis set. *Comput. Mater. Sci.* **1996**, *6* (1), 15−50.
(34) Grimme, S.; Antony, J.; Ehrlich, S.; Krieg, H. A consistent and accurate ab initio parametrization of density functional dispersion correction (DFT-D) for the 94 elements H-Pu. *J. Chem. Phys.* **2010**, *132* (15), No. 154104, DOI: 10.1063/1.3382344.
(35) Huang, H. J.; Yan, M. M.; Yang, C. Z.; He, H. Y.; Jiang, Q. G.; Yang, L.; Lu, Z. Y.; Sun, Z. Q.; Xu, X. T.; Bando, Y.; Yamauchi, Y. Graphene Nanoarchitectonics: Recent Advances in Graphene-Based Electrocatalysts for Hydrogen Evolution Reaction. *Adv. Mater.* **2019**, *31* (48), No. 1903415, DOI: 10.1002/adma.201903415.
(36) Nørskov, J. K.; Bligaard, T.; Logadottir, A.; Kitchin, J. R.; Chen, J. G.; Pandelov, S.; Norskov, J. K. Trends in the exchange current for hydrogen evolution. *J. Electrochem. Soc.* **2005**, *152* (3), J23−J26.
(37) Chakarova-Käck, S. D.; Schröder, E.; Lundqvist, B. I.; Langreth, D. C. Application of van der Waals density functional to an ex-tended system: Adsorption of benzene and naphthalene on graphite. *Phys. Rev. Lett.* **2006**, *96* (14), No. 146107, DOI: 10.1103/PhysRevLett.96.146107.
(38) Coello-Fiallos, D.; Tene, T.; Guayllas, J. L.; Haro, D.; Haro, A.; Vacacela Gomez, C. DFT comparison of structural and electronic properties of graphene and germanene: monolayer and bilayer systems. *Mater. Today: Proc.* **2017**, *4* (7), 6835−6841.
(39) Hess, P. Thickness of elemental and binary single atomic monolayers. *Nanoscale Horiz.* **2020**, *5* (3), 385−399.
(40) Chen, X.; Tian, F.; Persson, C.; Duan, W.; Chen, N. X. Interlayer interactions in graphites. *Sci. Rep.* **2013**, *3*, No. 3046.
(41) Herrero, C. P.; Ramírez, R. Elastic properties and mechanical stability of bilayer graphene: molecular dynamics simulations. *Eur. Phys. J. B* **2023**, *96* (11), No. 147, DOI: 10.1140/epjb/s10051-023-00616-w.
(42) Rocha, A. R.; Padilha, J. E.; Fazzio, A.; da Silva, A. J. R. Transport properties of single vacancies in nanotubes. *Phys. Rev. B* **2008**, *77* (15), No. 153406, DOI: 10.1103/PhysRevB.77.153406.
(43) Qu, Y. T.; Wang, L. G.; Li, Z. J.; Li, P.; Zhang, Q. H.; Lin, Y.; Zhou, F. Y.; Wang, H. J.; Yang, Z. K.; Hu, Y. D.; Zhu, M. Z.; Zhao, X. Y.; Han, X.; Wang, C. M.; Xu, Q.; Gu, L.; Luo, J.; Zheng, L. R.; Wu, Y. E. Ambient Synthesis of Single-Atom Catalysts from Bulk Metal via Trap-ping of Atoms by Surface Dangling Bonds. *Adv. Mater.* **2019**, *31* (44), No. 1904496, DOI: 10.1002/adma.201904496.
(44) Centrone, A. Probing the paramagnetic interactions between the unpaired electronic spins of carbon atoms and the nuclear spins of hydrogen molecules with Raman spectroscopy. *J. Raman Spectrosc.* **2011**, *42* (12), 2165−2167.
(45) Valencia, A. M.; Caldas, M. J. Single vacancy defect in graphene: Insights into its magnetic properties from theoretical modeling. *Phys. Rev. B* **2017**, *96* (12), No. 125431, DOI: 10.1103/PhysRevB.96.125431.

https://doi.org/10.1021/acsomega.4c00495
ACS Omega 2024, 9, 16592−16600